



The impact of aging environment on the evolution of Al_2O_3 supported Pt nanoparticles and their NO oxidation activity

Santhosh Kumar Matam ^{a,*}, Evgenii V. Kondratenko ^b, Myriam H. Aguirre ^a, Paul Hug ^{a,1}, Daniel Rentsch ^c, Alexander Winkler ^d, Anke Weidenkaff ^a, Davide Ferri ^a

^a Empa, Swiss Federal Laboratories for Materials Science and Technology, Laboratory for Solid State Chemistry and Catalysis, Ueberlandstrasse 129, CH-8600 Duebendorf, Switzerland

^b Leibniz Institute for Catalysis at the University of Rostock, Albert-Einstein-Str. 29a, D-18059 Rostock, Germany

^c Empa, Swiss Federal Laboratories for Materials Science and Technology, Laboratory for Functional Polymers, Ueberlandstrasse 129, CH-8600 Duebendorf, Switzerland

^d Empa, Swiss Federal Laboratories for Materials Science and Technology, Laboratory for Internal Combustion Engines, Ueberlandstrasse 129, CH-8600 Duebendorf, Switzerland

ARTICLE INFO

Article history:

Received 14 June 2012

Received in revised form

12 September 2012

Accepted 13 September 2012

Available online 19 September 2012

Keywords:

Diesel oxidation catalyst
Aging environment
Thermal aging
Chemical aging
Phosphorus poison
Pt nanoparticles
Particle size
Particle morphology
NO oxidation
Structure sensitivity

ABSTRACT

The impact of the aging environment on the size, morphology and distribution of Pt nanoparticles supported on Al_2O_3 and on their NO oxidation activity is studied. To this end, the fresh catalyst Pt/ Al_2O_3 (Pt/Al/F) is aged under different aging environments mimicking the aging process of a real diesel oxidation catalyst (DOC) including phosphorus (P) poison as a chemical contaminant. These catalysts are characterized by N_2 -physisorption, CO chemisorption, XRD, solid state ^{27}Al MAS NMR, HAADF-STEM, HR-TEM, EDX analyses and CO-DRIFTS. The characterization results reveal that the thermal aging in air at 800 °C leads to a heterogeneous size and spatial distribution of Pt nanoparticles in the catalyst (Pt/Al/O). The morphology is mainly limited to truncated cubic structures that are dominated with (100) crystal facets. Differently, aging in a lean diesel exhaust environment (Pt/Al/R) restricts the extensive Pt particle growth, size distribution to narrow and morphology predominantly to cuboctahedral that contains both (111) and (100) planes, though the former tends to dominate the surface. P seems to control both the growth of Pt particles and the morphology that is mainly limited to spherical irrespective of the aging environment (P/Pt/Al/O or P/Pt/Al/R). The normalized (per surface Pt atoms) forward rate constant of NO oxidation and the corresponding activation energy are determined for the differently treated catalysts and compared them with those reported in previous relevant studies. From these results it is evident that the reaction is indeed structure sensitive. The catalyst treated in lean diesel exhaust environment (Pt/Al/R) presents the best activity followed by the fresh Pt/Al/F and thermally Pt/Al/O aged catalysts. The difference in the NO oxidation activity of the catalysts is attributed to the morphology of Pt nanoparticles. These results correlate very well with the real DOC monolith that was aged on a heavy duty small truck for 250 h under different driving profiles.

© 2012 Elsevier B.V. All rights reserved.

1. Introduction

Nitrogen oxides (NO_x) are considered harmful to the public health and the environment thus their emissions are strictly regulated, especially in Europe with stringent Euro VI and EEV legislations. Catalytic converters play a crucial role to mitigate NO_x emissions from lean burn diesel engines. For such applications, a diesel oxidation catalyst (DOC) comprising of platinum supported on alumina is typically used in combination with a diesel particulate filter (DPF) and NO_x storage reduction (NSR) or selective catalytic reduction of NO_x (SCR) catalyst. The exhaust from the engine first

passes through the DOC (front part of the after-treatment system) where oxidation of CO, unburned hydrocarbons and NO takes place. Then particulate matter of the exhaust is filtered in DPF followed by the reduction of NO_x at NSR/SCR catalyst (rear part of the system). In this after-treatment system, the efficiency and durability of DOC is the key as it catalyzes NO oxidation reaction (Eq. (1)) that affects the rate and selectivity of NO_x reduction in SCR, NO_x storage capacity in NSR and passive regeneration of DPF by NO_2 [1–3].



Therefore, the role of different factors such as the influence of aging (thermal and chemical) and of Pt particle size and shape on the DOC performance has been a topic of research [1–12]. Thermal aging can be the result of active regeneration of DPF that clogs with soot over time. The regeneration is typically performed by burning excess diesel fuel within the DOC during which typical diesel

* Corresponding author. Tel.: +41 58 765 4726; fax: +41 58 765 4019.

E-mail address: santhosh.matam@empa.ch (S.K. Matam).

¹ Deceased 24th November 2011.

exhaust gas temperatures (400 °C) can exceed by far (up to 900 °C). These high temperature excursions induce physical changes in DOC such as decrease in the surface area of the support and Pt that in turn results in reduced catalytic activity [11–14].

Chemical aging is mainly caused by the decomposition of lube oil and fuel additives leading to phosphorus (P), sulphur (S), zinc (Zn), magnesium (Mg) and calcium (Ca) deposition on DOC. Such contaminants can strongly interact with the support alumina and Pt nanoparticles thus decreasing the catalyst efficiency and durability significantly [7,10,11,14]. Our previous studies on DOC monolith of a heavy duty small truck diesel engine have shown that chemical contaminants P and Zn originating from the anti-wear and engine oil additives like zinc-dialkyldithiophosphates (ZDDP) deposit heavily with time on it leading to catalyst deactivation [14]. It was observed that there is a concentration gradient of P along the DOC monolith. The highest concentration of P is at the inlet region (close to the engine) of DOC (denoted as DOC_{in}) and decreases with the length showing either no or minimal amount of P depending on the mileage at the rear part of DOC (DOC_{out}). Additionally, temperature and concentration gradients of the exhaust pollutants (reactants) and their products exist along the DOC. High concentrations of the exhaust pollutants and relatively low temperatures prevail at the inlet of DOC_{in} , whereas the rear part (DOC_{out}) is exposed mostly to the products and relatively high temperatures. However, the role of concentration and temperature gradients along the DOC in the aging process is not understood and hence, the NO oxidation efficiency of the DOC along the length is not known. This is due to the fact that previous studies mainly focus on the macro and micro structural changes of the model DOC catalysts such as support phase transformation upon P poisoning, zeolite crystal structure alterations and Pt dispersion. The effect of these changes on the CO and hydrocarbon (mainly propane or propylene) oxidation efficiency, however not on the NO oxidation activity, has been studied [7,10,11]. Furthermore, oxidation of NO with O_2 over supported and unsupported Pt nanoparticles is contentiously discussed [1–8,12,14–16]. Some theoretical and experimental studies have demonstrated that NO oxidation is structure sensitive showing improved activity with increased Pt particle size [3,4,6,8,15]. In contrast, a study on the oxidation of NO with O_2 on large single crystals of Pt(111) and Pt(321) concludes that the reaction is not structure sensitive [2].

To the best of our knowledge, there are no studies dealing with the elucidation of the aging effect of supported Pt catalysts treated under DOC relevant environments, on their structural and catalytic properties. Therefore, the aim of the work is to understand the effect of aging environment on NO oxidation at a fundamental level. To this end, differently aged Pt/Al₂O₃ catalysts are thoroughly characterized for understanding the structure and morphology as well as for determining intrinsic activity of NO oxidation with O_2 . The results demonstrate that the evolution of supported Pt nanoparticles is a function of aging environment and it significantly determines the Pt normalized constant of NO. These experiments provide a basis for understanding the NO conversion behavior along the DOC monolith aged on a heavy duty small truck engine for 250 h under different driving profiles [14].

2. Experimental

2.1. Catalysts and aging procedure

2 wt% Pt/Al₂O₃ powder (a model DOC) was kindly provided by Umicore AG. The catalyst was calcined in air at 500 °C for 4 h, named as Pt/Al/F. The fresh catalyst was then thermally aged in a muffle furnace in flowing air at 800 °C for 5 h (denoted as Pt/Al/O). A portion of fresh catalyst (200 mg) was also treated in a

plug-flow reactor under simulated lean diesel exhaust gas mixture (feed composition: 3000 ppm CO, 250 ppm NO, 1200 ppm C₃H₆, 300 ppm C₃H₈, 11 vol% O₂, 25 vol% CO₂ in N₂) with a flow rate of 200 ml/min at 800 °C for 5 h (labelled as Pt/Al/R). To study the influence of chemical contaminants namely phosphorus (P) on DOC performance, the fresh catalyst powder was impregnated with P from an aqueous (NH₄)₃PO₄ solution and dried at 120 °C overnight. Then, it was either thermally aged in a muffle furnace in air (Pt/Pt/Al/O) or in a plug-flow reactor under simulated exhaust gas atmosphere at 800 °C for 5 h (Pt/Pt/Al/R). The phosphorus content (7.5 wt% P) was determined by energy dispersive X-ray (EDX) analysis during STEM measurements. Pt content in the catalysts was validated by ICP-OES. Physico-chemical properties of the catalysts are presented in Table 1.

2.2. Characterization techniques

2.2.1. N₂-physisorption

Nitrogen adsorption and desorption isotherms at –196 °C were obtained on a Micromeritics ASAP 2020c instrument. Prior to the experiments, the catalysts were pretreated at 350 °C for 2 h. The total surface area of the samples was determined by the BET method.

2.2.2. Solid state ²⁷Al MAS NMR

Single pulse NMR experiments were performed (at 104.26 MHz) at room temperature on a Bruker Avance 400 NMR spectrometer using a 2.5 mm CP/MAS probe (at spinning rates of 25,000 Hz). The ²⁷Al chemical shifts were referenced to an external sample of aluminum nitrate solution (1.1 M).

2.2.3. CO-chemisorption

Experiments were performed on a Micromeritics ASAP 2020c instrument. Catalysts were evacuated at 100 °C for 30 min and reduced in hydrogen at 350 °C for 2 h. At the same temperature, catalysts were evacuated for 2 h followed by cooling down to 35 °C. At this temperature, CO chemisorption was carried out.

2.2.4. X-ray diffraction (XRD)

The powder XRD patterns of the catalysts were obtained on a PANalytical X'Pert PRO θ -2 θ scan system (Johansson monochromator and a X'Celerator linear detector) using Cu K α_1 (1.5406 Å, 45 kV and 40 mA). XRD data were collected in the range of 10–80° (2 θ) using a step size of 0.0167° and a step time of 50 s.

2.2.5. Transmission electron microscopy

High angular annular dark field scanning transmission electron microscopy (HAADF-STEM) and high resolution transmission electron microscopy (HR-TEM) were acquired on a JEOL FS2200-FEG operating at 200 kV. The catalysts were dispersed in deionized water, dropped on carbon-film coated copper grids and dried in air. Particle size distribution was evaluated from the STEM images using the Digital Micrograph software from Gatan Inc and was determined from counting 150 to 250 Pt nanoparticles. The resulting average particle size in the catalysts is reported in Table 1.

2.2.6. CO adsorbed diffuse reflectance infrared Fourier transform spectroscopy (CO-DRIFTS)

CO-DRIFTS experiments were performed on a VERTEX 70 FT-IR spectrometer (Bruker Optics) equipped with a diffuse reflectance accessory (Praying Mantis, Harrick) and a liquid nitrogen cooled MCT detector. The catalysts were pre-treated in 10 vol% H₂/He at 200 °C for 30 min. Subsequently cooled to room temperature and purged with He flow for few minutes. Then CO adsorption (5 vol% CO/He) was carried out. Difference spectra were recorded at room temperature by co-adding 200 scans at a resolution of 4 cm^{–1}. The

Table 1

Physico-chemical properties of the catalysts are compared with the literature. Activation energies (E_a) for NO oxidation are calculated from the Arrhenius plot of the forward rate constant reported in Fig. 7(a).

Catalysts	S_{BET} ($m^2 g^{-1}$) ^a	V_{Total} ($cm^3 g^{-1}$) ^b	CO-Chem. (D%) ^c	I (a.u.) ^d	Particle size (nm)			E_a (kJ mol ⁻¹)	[Ref]
					CO-Chem. ^c	XRD ^e	STEM ^f		
Pt/Al/F	140	0.47	11.5	21.15	10	–	4.2(1.5)	112.5 ± 5	†
Pt/Al/O	133	0.47	2.3	2.08	50	34	6.7(6.0)	115.3 ± 9	†
Pt/Al/R	138	0.47	7.5	14.35	15	–	5.5(3.4)	95.6 ± 10	†
P/Pt/Al/O	70	0.27	–	–	32	6.3(6.1)	141.6 ± 19	†	
P/Pt/Al/R	55	0.19	0.88	1.28	129	14	5.6(0.5)	127.7 ± 19	†
Pt(0.3 wt%)/Al ₂ O ₃	–	–	42 [‡]	–	2.0 [‡]	–	–	39	[31]
Pt(0.1 wt%)/Al ₂ O ₃	197	–	72 [‡]	–	1.1 [‡]	–	–	–	[5]
Pt(0.27 wt%)/Al ₂ O ₃	126 [*]	0.49 [*]	82 [‡]	–	1.0 [‡]	–	–	–	[6]
Pt(0.3 wt%)/Al ₂ O ₃	126 [*]	0.49 [*]	4.4 [‡]	–	18.6 [‡]	–	–	–	[6]

^a BET method; ^{*} reported only for bare support alumina.

^b Based on BJH desorption isotherm.

^c CO-chemisorption (Pt to CO ratio of 1:1 was used). [‡] H₂-chemisorption and particle size is determined by $d(\text{nm}) = 0.821/D$ (D = dispersion) [5].

^d (I) corresponds to integral intensity of CO-DRIFTS of the catalysts reported in Fig. 6.

^e Based on the Scherrer equation.

^f Standard deviation is shown in the parenthesis. [†] Present work.

integral intensity (I (a.u.)) of linear and bridge bound CO bands observed in the spectra of studied catalysts is obtained by the OPUS 6.5 software, Bruker Optik GmbH.

2.2.7. Activity tests

NO oxidation activity was determined in a quartz tube reactor (12 mm internal diameter and 40 cm length). The reactor was loaded with 50 mg of catalyst (sieve fraction of 150–200 μm) diluted with quartz particles of the same size. Prior to reaction, catalysts were pretreated at 300 °C in a flow of 10% O₂/N₂ for 1 h to remove adsorbed gaseous molecules from the surface and subsequently cooled to 50 °C. Then, the reaction mixture (400 ppm NO, 10 vol% O₂, balance N₂ at 700 ml/min) was introduced at a gas hourly space velocity (GHSV) of 92,840 h⁻¹. The reaction was performed between 50 and 500 °C with a heating rate of 5 °C/min. Product evolution was followed by FT-IR (Thermo Nicolet 5700 equipped with an Axiom gas cell).

3. Results and discussion

3.1. N₂-physisorption

The total surface area and pore volume of the series of catalysts are presented in Table 1. The N₂ adsorption–desorption isotherms of the catalysts represent the type IV with a well-defined hysteresis loop of type H1, which is typically observed for such materials [17,18]. Pt/Al/F, Pt/Al/O and Pt/Al/R show comparable surface area and pore volume suggesting that high temperature treatment either in air or in lean exhaust environment does virtually not affect the physical and textural properties of the support alumina of the catalysts (Table 1). However, P aged catalysts P/Pt/Al/O and P/Pt/Al/R show dramatic loss in both surface area and pore volume as compared to their counter parts Pt/Al/O and Pt/Al/R without P, respectively. This indicates that P is located on the surface and within the pores of the support alumina.

3.2. Solid state ²⁷Al MAS NMR

Solid state ²⁷Al NMR spectra of reference aluminum phosphate and pristine γ -Al₂O₃ support are compared with P aged catalyst P/Pt/Al/O in Fig. 1. Aluminum phosphate shows a peak at 39.33 ppm that is typically attributed to Al³⁺ of AlPO₄ [19,20]. The spectrum of pristine γ -Al₂O₃ exhibits well known peaks at 7.17 and 54.25 ppm, which are often assigned to Al³⁺ in octahedral and tetrahedral

coordination, respectively [19]. Based on this, it can be seen that the intensity and the peak position of octahedrally coordinated Al³⁺ are essentially the same for pristine γ -Al₂O₃ and P/Pt/Al/O. However, the intensity of tetrahedrally coordinated Al³⁺ decreases considerably and a new intense peak at 37.31 ppm emerges indicating that P preferentially reacts with tetrahedrally coordinated Al³⁺ ions to form AlPO₄ like species [20]. These results are in line with N₂-physisorption data that show decreased surface area and pore volume for P aged catalysts.

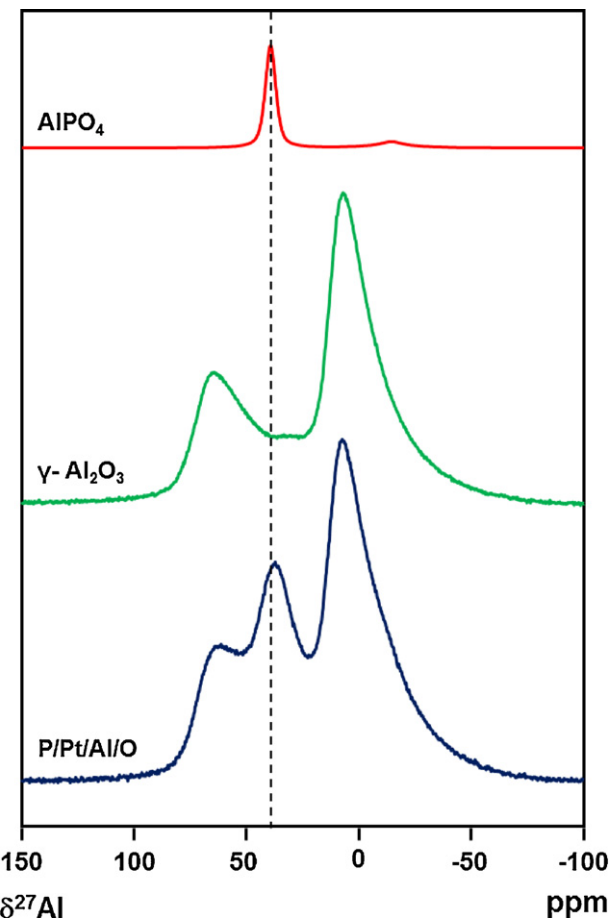


Fig. 1. 1D ²⁷Al MAS NMR spectra (104.26 MHz) of the reference samples and the catalyst.

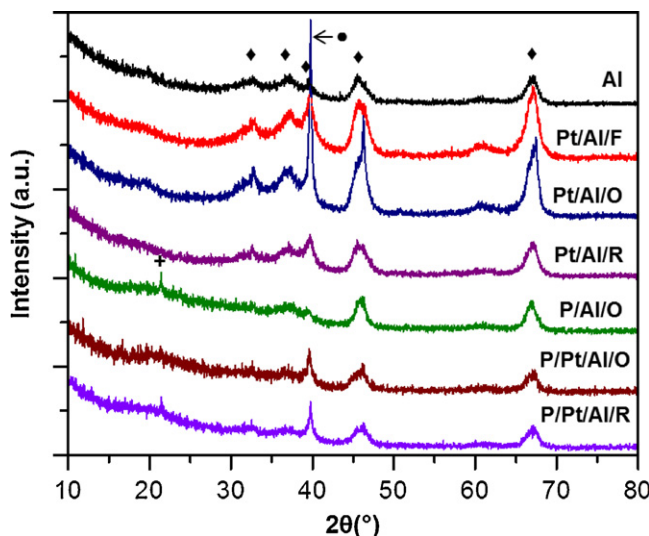


Fig. 2. XRD patterns of the pristine and P aged alumina supports and catalysts: (◆) γ -Al₂O₃, (●) metallic Pt and (+) AlPO₄.

3.3. CO-chemisorption

CO chemisorption data show that the dispersion of Pt in the catalysts decreases upon aging (Table 1). The fresh catalyst Pt/Al/F exhibits the highest Pt dispersion followed by Pt/Al/R, Pt/Al/O, P/Pt/Al/R and P/Pt/Al/O. Among the P free catalysts, Pt/Al/O shows the lowest Pt dispersion which can be attributed to the loss of surface Pt sites upon aging in air. Interestingly, the loss of surface Pt sites is not so severe for catalyst Pt/Al/R that was aged under lean exhaust environment as compared to Pt/Al/O. It is noteworthy that both the catalysts Pt/Al/O and Pt/Al/R are aged at 800 °C, however under different environments which could be responsible for the observed differences in the surface Pt sites. It appears that the decrease in the Pt dispersion is even more severe for P aged catalyst P/Pt/Al/R as compared to P free catalyst Pt/Al/R (Table 1). This should be treated with caution because a fraction of P might have deposited on Pt nanoparticles (i.e. fouling) that can also decrease the number of surface Pt sites for CO adsorption which in turn result in the decreased Pt dispersion. Therefore, the dispersion data is further assessed by XRD which is sensitive to the bulk volume of the Pt particles rather than surface Pt.

3.4. X-ray diffraction

XRD diffractograms of the catalysts are compared with pristine γ -Al₂O₃ (Al) and P aged (P/Al/O) alumina supports in Fig. 2. The pristine Al support shows reflections at 2θ of 32.6°, 37.2°, 39.4°, 45.5° and 67.1° which are characteristic for the γ -Al₂O₃ phase [17,18]. These reflections can still be seen for the catalysts Pt/Al/F, Pt/Al/O and Pt/Al/R. However, sharp reflections at 2θ of 39.8° and 46.2° appear besides the γ -Al₂O₃ phase reflections for Pt/Al/O which can be attributed to metallic Pt particles [21,22]. These reflections are very weak and are obscured by the dominant alumina support reflections for the catalysts Pt/Al/F and Pt/Al/R, indicating that the size of Pt particles are smaller in the catalysts than those in Pt/Al/O. Interestingly, support Al reflections at 2θ of 32.6°, 37.2° and 39.4° almost disappear while those at 2θ of 45.5° and 67.1° do virtually not change for P aged support P/Al/O and catalysts. Additionally, a new reflection appears at 2θ of 21.4° which can be attributed to the aluminum phosphate phase [19]. These results again suggest that P reacts with the support Al and forms aluminum phosphate like phase, consistent with NMR results. Besides this, it can also be clearly seen that P/Pt/Al/O and P/Pt/Al/R show a sharp reflection at

2θ of 39.8°, which is similar to the one observed for Pt/Al/O and is assigned to metallic Pt particles. By using the peak fitting method, the full width half-maximum (FWHM) of the peak at 2θ of 39.8° could be determined only for Pt/Al/O, P/Pt/Al/O and P/Pt/Al/R by almost eliminating the support contribution to the reflection. The resulting average Pt particle size in the catalysts Pt/Al/O, P/Pt/Al/O and P/Pt/Al/R is 34, 32 and 14 nm, respectively (Table 1). It is noteworthy that the XRD reflections assignable to neither α -, δ - or θ -Al₂O₃ phases [23,24] nor PtO_x phases [25] are present. This suggests that aging (without P) the fresh Pt/Al/F catalyst at 800 °C either in air or in lean exhaust environment does not change the catalyst composition, in good agreement with N₂-pysisorption results. The average particle size determined by XRD differs significantly from that estimated by CO chemisorption (Table 1). This discrepancy can be attributed to the sensitivity (volume vs surface) of the techniques and is frequently discussed in the literature [21,22,26,27]. Having said that, the particle size distribution determined by XRD follows the same trend as that estimated from CO chemisorption for P free catalysts. However, CO chemisorption on P aged catalyst P/Pt/Al/R shows an unprecedented particle size distribution due to fouling of Pt particle surface by P. To obtain rational results on the Pt particle size distribution, the catalysts are further analyzed by transmission electron microscopy which is complementary to XRD and CO chemisorption.

3.5. Transmission electron microscopy

High angular annular dark field (HAADF) STEM images of the catalysts Pt/Al/F, Pt/Al/O and Pt/Al/R as well as the respective size distribution of Pt nanoparticles are depicted in Fig. 3. As evident from the STEM image and histogram, the fresh catalyst contains more or less homogeneous size and spatial distribution of Pt nanoparticles. The average Pt particle size is determined to be around 4.2 nm (Table 1). Thermal aging of the fresh catalyst results in decreased Pt dispersion in Pt/Al/O. From the STEM image and histogram of thermally aged Pt/Al/O (Fig. 3), it can be seen that the size and spatial distribution of Pt nanoparticles become heterogeneous. The size of larger Pt particles is between 5 and 50 nm with an average size of around 6.7 nm (Table 1). In a marked contrast, aging under lean exhaust conditions retains almost the homogeneous size and spatial distribution of Pt nanoparticles in Pt/Al/R as observed for the fresh catalyst Pt/Al/F (Fig. 3). However, the mean Pt particle size increases from 4.2 nm of the fresh catalyst to 5.5 nm for Pt/Al/R (Table 1). Aging under lean exhaust environment restricts the growth of Pt nanoparticles to well below 18 nm and confines the size distribution mainly to a narrow window as compared to thermal aging in air that favors extensive particle growth and a wide size distribution. These results indicate that the aging conditions did influence the size and spatial distribution of Pt nanoparticles on the alumina support. As evident from Fig. 3 and Table 1, the average particle size in the catalysts Pt/Al/F, Pt/Al/R and Pt/Al/O is around 4, 5.5 and 6.7, respectively. This size range is within the detection limit of XRD. Therefore, Pt/Al/F and Pt/Al/R did not show any significant XRD reflections (Fig. 2) of Pt metal particles, while those reflections observed on Pt/Al/O are indeed due to a fraction of larger particles that are in the range of 5–50 nm as evident from Fig. 3. These observations confirm that XRD data do not represent the whole particle size distribution in the catalysts which in turn demonstrate that STEM is an important complementary technique for such studies. These results are partly corroborated by CO chemisorption that is sensitive to the local electronic/chemical properties of Pt sites (Table 1).

The influence of aging conditions on the morphology of Pt nanoparticles in the catalysts is studied by high resolution transmission electron microscopy (HR-TEM) (Fig. 4). The morphology of Pt nanoparticles in the fresh catalyst Pt/Al/F appears to be a

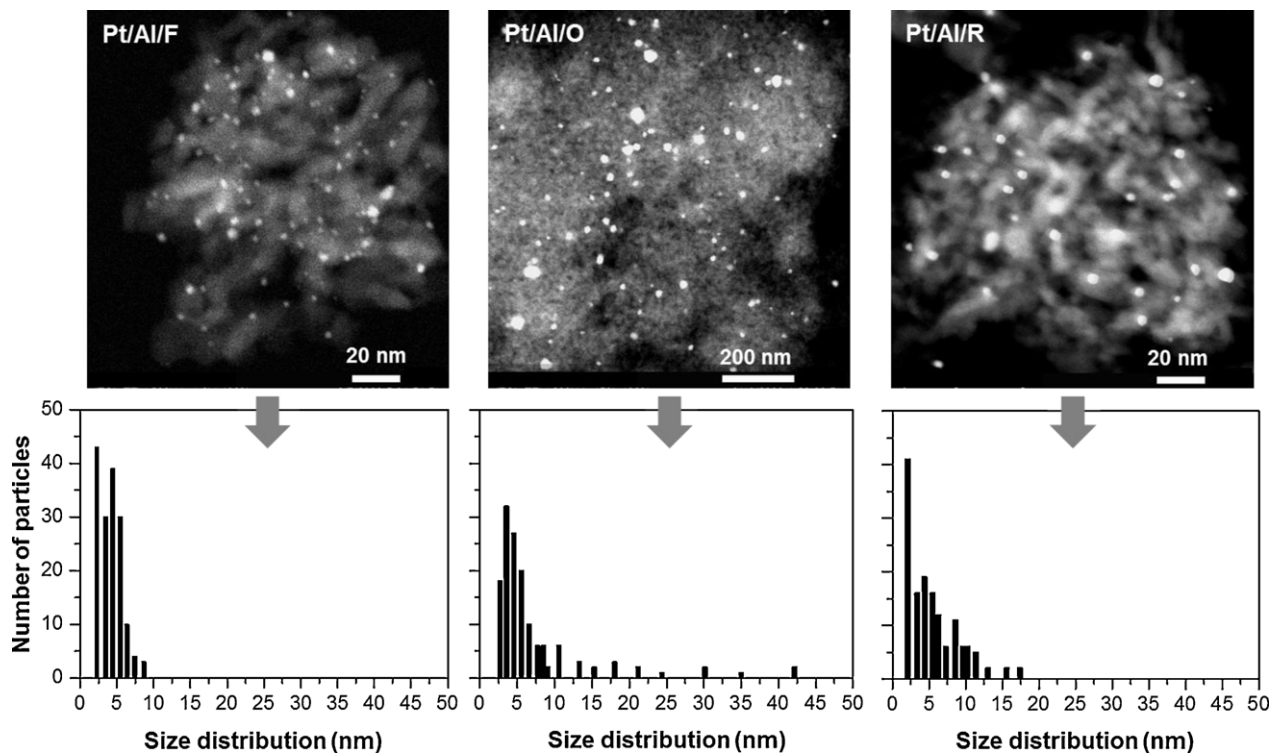


Fig. 3. Dark field STEM images (above) and histograms (below) of the catalysts.

mixture of cuboctahedral, cubic, irregular and spherical. Though the proportion of these particles is difficult to be derived, it can be seen in HR-TEM images that Pt nanoparticles which are in the mean size range of 4.2 nm are cuboctahedral (see the inset image), cubic or irregular and those well below the mean size (<2 nm) are mainly spherical (Fig. 4). In contrast, thermally aged catalyst Pt/Al/O contains mainly irregular and truncated Pt particles. In the latter case, truncated trigonal pyramid and truncated cubic structures like tetragonal are commonly observed (Fig. 4). The size of these Pt particles is between 5 (in the range of mean particle size) and 50 nm. Pt nanoparticles that are well below the mean size (<2 nm) remain spherical as in the fresh catalyst Pt/Al/F, though their population is decreased considerably in favor of larger ones upon thermal aging. This is reasonable because the fresh catalyst is the parent (starting) material of Pt/Al/O. It is noteworthy that the cuboctahedral Pt particles could not be detected in Pt/Al/O, however their presence cannot be ruled out. Remarkably, catalyst Pt/Al/R aged under lean exhaust environment contains well defined Pt crystal structures. These are mainly cuboctahedral Pt nanoparticles besides a fraction of spherical particles (Fig. 4). The former is observed in the whole size range detected in the catalyst while the latter is detected only in the size range of <2 nm. It should be noted that truncated Pt particles are not observed.

These results clearly demonstrate that the morphology of Pt nanoparticles supported on alumina strongly depends on the aging environment. Thermal aging under air flow (oxidizing environment) results in the formation of smoothed spherical, truncated and irregular Pt particles. Differently, aging under lean exhaust environment promotes mainly formation of cuboctahedral nanoparticles. This is in agreement with previous reports according to which the shape of Pt particles changes from cuboctahedral in the reducing reaction environment to a more spherical shape in an oxidizing environment [3,28,29]. Although the lean exhaust environment do not directly reflect the reducing environment of pure H₂ as reported in [29], the exhaust composition and products may be determining the Pt morphology in the catalyst. The morphology of Pt particles

is an important parameter as it determines the relative ratio of different surface Pt sites and facets of a crystal which can control the catalytic activity [30–32]. Pt nanoparticles with cubic, truncated cubic, truncated tetragonal and irregular shapes in Pt/Al/O mainly exhibit (100) facets. The observed truncated triangular or trigonal shapes predominately consist of (111) facets. Cuboctahedral Pt nanoparticles in Pt/Al/R consists of both (111) and (100) facets though the former tend to dominate the surface [3,29–32] (inset of Fig. 4). These results indicate that the surface Pt sites and facets of Pt nanoparticles in the catalysts are significantly different. This can explain the CO chemisorption results that show relatively larger Pt particles in the catalysts as compared to XRD and STEM (Table 1).

The influence of P, a chemical contaminant, in a combination with the aging environment (i.e., lean exhaust gas composition of a diesel engine) on the evolution of Pt nanoparticles on Al₂O₃ is studied to shed some light on the aging behavior of the inlet region of a DOC in diesel engines [14]. For comparative purposes, P in combination with aging environment of air is also investigated. The corresponding STEM, HR-TEM and histograms of catalysts P/Pt/Al/R and P/Pt/Al/O are shown in Fig. 5. Catalyst P/Pt/Al/R contains only spherical shape Pt nanoparticles. This is striking when compared to the catalyst Pt/Al/R (without P) that exhibits mostly cuboctahedral Pt nanoparticles. The average Pt particle size is slightly larger for P/Pt/Al/R than that for Pt/Al/R (see Table 1). However, the size distribution is relatively narrower for the former than that for the latter as evident from the relative population of Pt particles in the corresponding histograms (Figs. 3 and 5). These results indicate that P smoothes the sharp edges of Pt particles resulting in a more spherical shape. Interestingly, catalyst P/Pt/Al/O exhibits both spherical and truncated Pt nanoparticles. In this catalyst the proportion of spherical Pt particles is significantly higher than that of truncated ones. The latter are mainly large Pt particles which are well above the average particle size of 6.3 nm. Again, this is a different observation from that of Pt/Al/O (without P) which contains mainly truncated Pt nanoparticles. The size distribution of Pt nanoparticles is relatively narrower for P/Pt/Al/O than for Pt/Al/O

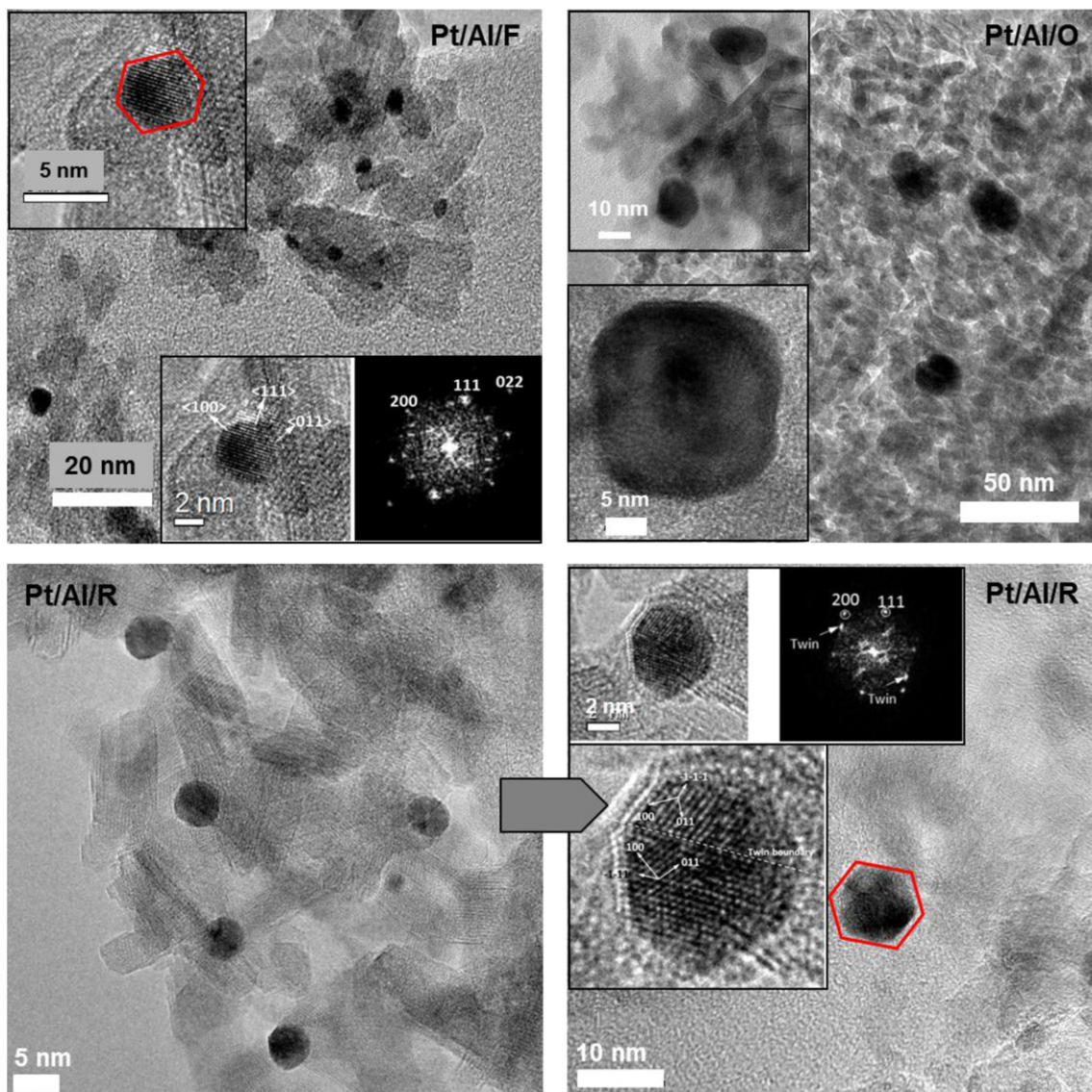


Fig. 4. HR-TEM images of the catalysts. Fast Fourier transform (FFT)-diffraction patterns of Pt nanoparticles and crystal planes as well as particle morphology are shown in the insets. Cuboctahedral Pt nanoparticles are marked with red border. (For interpretation of the references to color in this figure legend, the reader is referred to the web version of the article.)

(Figs. 3 and 5). From these results it is evident that P and the aging environment do play a vital role in the evolution of Pt nanoparticles. P seems to interact with Pt nanoparticles and alters their morphology from a crystal structure to spherical. This process is more effective in the lean exhaust gas environment than in air. These results are in good agreement with our previous observations on a real DOC monolith of a heavy duty small truck diesel engine aged for 250 h [14]. The morphology of Pt nanoparticles is observed to be spherical at the inlet region of the DOC (DOC_{in}), as in $Pt/Pt/Al/R$, exposed mainly to lean exhaust pollutants (reactants) and where heavy P contamination is detected. The rear part of the DOC monolith (DOC_{out}), which is almost free from P contamination and is mainly exposed to products, exhibits large truncated Pt particles as observed for $Pt/Al/O$. These results on the evolution of Pt nanoparticles morphology as a function of aging environment in the model catalysts and in the real DOC monolith are in line with literature that report the effect of reaction environment on the morphology [28,29]. Reversible shape transformation of Pt particles under redox cycles was demonstrated by environmental transmission electron microscopy (ET-EM). The square Pt particles were transformed to

almost cuboctahedral by changing from oxidizing environment to reducing atmosphere [29]. Similarly, it was found that by changing the atmosphere from reducing to oxidizing cuboctahedral Pt nanoparticles transform to a more spherical shape [28]. It is evident from Table 1 that the trend in the particle size distribution in P aged catalysts determined by XRD and STEM is the same, however CO chemisorption does not represent this trend due to fouling of Pt particle surface by P.

3.6. CO-DRIFTS

The morphology of Pt particles in the catalysts is further investigated by CO-DRIFTS by probing C–O vibrational modes [$\nu(CO)$] which are sensitive to the adsorption site structure of Pt nanoparticles and hence different crystal planes can be identified. DRIFTS spectra of the catalysts after adsorption of CO followed by flushing with He for 30 min are shown in Fig. 6. It can be readily seen that there are striking differences between the adsorbed $\nu(CO)$ modes on the catalysts. Additionally, the integral intensity of the spectra decreases for the catalysts upon aging (Table 1). These observations

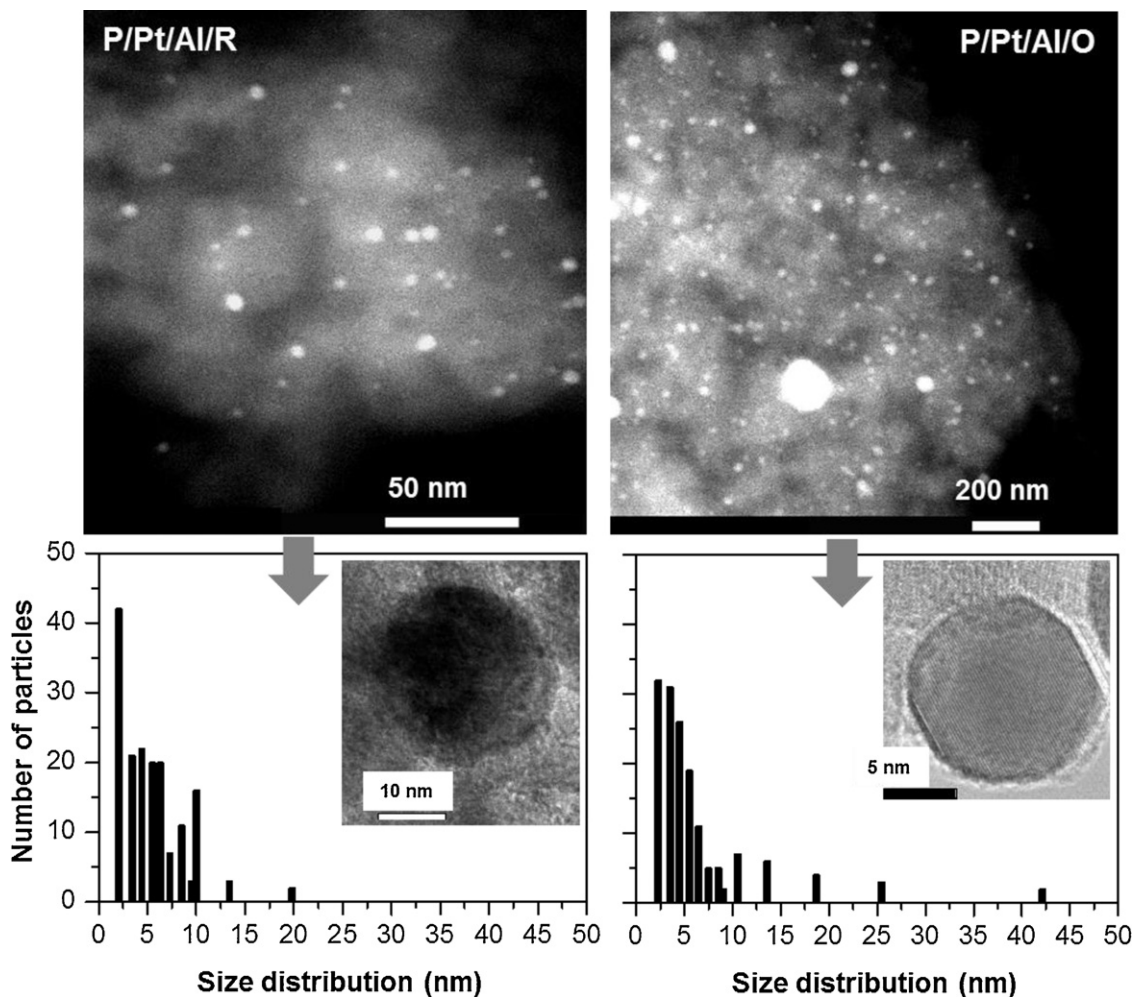


Fig. 5. Dark field STEM images (above) and histograms (below) of the catalysts: as an example, HR-TEM images of a spherical particle is shown in the insets.

infer that the proportion of different surface Pt sites on nanoparticles is different in the catalysts. The fresh catalyst Pt/Al/F exhibits two intense bands at 2086 and 2067 cm^{-1} and a broad band at 1834 cm^{-1} . The intensity of the bands at 2086 and 2067 cm^{-1} is

different; the latter is more intense than the former. This indicates that the fraction of surface Pt sites responsible for the two bands is not the same. These two bands are often attributed to linearly adsorbed CO ($\nu(\text{CO}_L)$) mode, however on different surface Pt sites [33–40]. The band at around 2086 cm^{-1} is contentiously assigned to both terrace Pt(1 1 1) and Pt(1 0 0) [33–40]. Based on single crystals Pt(1 1 1) and Pt(1 0 0) studies, the band at 2086 cm^{-1} is tentatively attributed to CO linearly bound to Pt atoms on terrace (1 1 1) [33,36]. Having said this, a contribution from $\nu(\text{CO}_L)$ mode on Pt (1 0 0) atoms cannot be ruled out as the band position and intensity sensitively depends on the surface CO coverage at any given temperature [33–36,40]. Whilst, the band at 2067 cm^{-1} is unambiguously ascribed to coordinatively unsaturated Pt atoms such as at steps, edges and kinks of Pt nanoparticles [33–40]. The intensity difference between these two intense bands suggests that the fraction of coordinatively unsaturated Pt sites is higher than saturated terrace atoms in the catalyst. In agreement with this, a band at 1834 cm^{-1} is observed which is due to bridge bound CO ($\nu(\text{CO}_B)$) mode at coordinatively unsaturated Pt sites [34,35,38–40]. These results are in excellent agreement with STEM and HR-TEM observations showing the presence of small Pt nanoparticles with an average size of 4.2 nm and with different shapes including cuboctahedral, cubic, spherical and irregular (inset of Fig. 4).

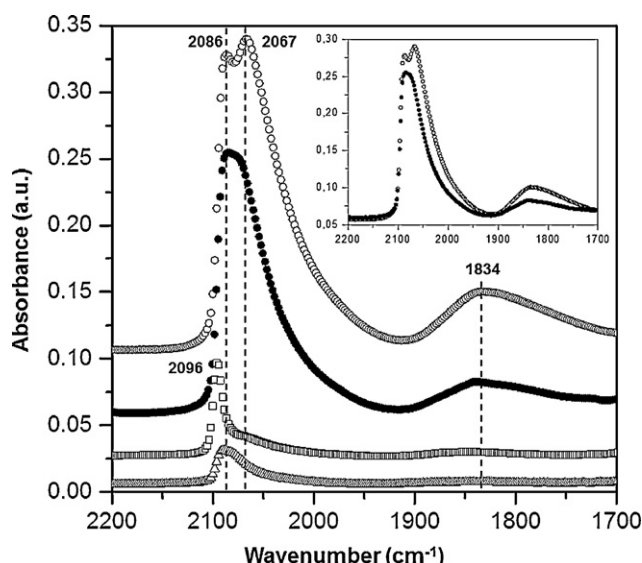


Fig. 6. DRIFT spectra of CO adsorbed at room temperature: Pt/Al/F (○), Pt/Al/R (●), Pt/Al/O (□) and P/Pt/Al/R (△). For the sake of clarity, spectra of Pt/Al/F (○) and Pt/Al/R (●) are compared in the inset.

Significantly, catalyst Pt/Al/R that contains mainly cuboctahedral Pt nanoparticles with a mean size of 5.5 nm as evidenced by STEM and HR-TEM shows essentially two bands: an intense band at 2085 cm^{-1} and a broad band at 1838 cm^{-1} . The most intense band at 2067 cm^{-1} observed for the fresh catalyst Pt/Al/F is now

merely present as a shoulder at the low frequency tail (see inset) of the intense band of 2085 cm^{-1} . The intensity of the broad band at 1838 cm^{-1} is attenuated compared to the fresh catalyst Pt/Al/F. These results suggest that upon aging under lean exhaust environment the surface Pt structure is more ordered than that in the fresh catalyst, implying decreased coordinatively unsaturated surface Pt sites in favor of terrace Pt atoms such as (1 1 1) and (1 0 0), in excellent agreement with the microscopic studies (see inset of Fig. 4). In a marked contrast, catalyst Pt/Al/O aged under air flow presents only a band at 2096 cm^{-1} with a weak shoulder at 2067 cm^{-1} . And, the broad $\nu(\text{CO}_\text{B})$ band at 1838 cm^{-1} observed for both Pt/Al/F and Pt/Al/R is almost missing in Pt/Al/O. The absolute intensity of the spectrum is much lower than that of Pt/Al/F and Pt/Al/R, which is also evident from the integral intensity of the spectra reported in Table 1, in agreement with CO chemisorption data. These results indicate that the population of reactive surface Pt sites decreases considerably in favor of relatively larger particles containing coordinatively saturated Pt sites [37]. HR-TEM data (Fig. 4) show that the morphology of Pt particles is mainly irregular and truncated trigonal pyramid and cubic structures, which possess principally (1 0 0) facets with probably low surface area like in single crystals. Therefore, the band at 2096 cm^{-1} is tentatively attributed to the $\nu(\text{CO}_\text{L})$ mode arising upon adsorption of CO on coordinatively saturated Pt sites of extended (1 0 0) facets [33,37]. These crystal facets might be responsible for low CO uptake at room temperature by the catalysts Pt/Al/O as observed by CO-DRIFTS and CO chemisorption, which ultimately manifest large Pt particles in the catalyst (Table 1).

Interestingly, P/Pt/Al/R exhibits only one band at 2086 cm^{-1} and the bands corresponding to coordinatively unsaturated Pt sites at 2067 and 1834 cm^{-1} are missing. Despite higher Pt dispersion in P/Pt/Al/R than in Pt/Al/O as evidenced by XRD and STEM (Figs. 3 and 5 and Table 1), the intensity of the $\nu(\text{CO}_\text{L})$ band of P/Pt/Al/R is similar (if not lower) to the one observed for Pt/Al/O. These results again indicate that P deposits heavily on Pt nanoparticles, especially on coordinatively unsaturated Pt sites, in agreement with CO chemisorption results that show a very low CO uptake (Table 1). This is further supported by EDX analyses that show the presence of P on Pt particles (Fig. S1). Deposited P on nanoparticles prevents access for adsorption of CO on Pt sites. This result in a very small fraction of surface Pt sites that are available for CO adsorption, as evident from the integral intensity of the spectrum and CO chemisorption results reported (Table 1).

3.7. Activity tests

The effect of Pt particle size, distribution and morphology on NO oxidation in excess of O_2 (without NO_2 in the feed) is assessed in the temperature range between 50 and 500°C . Due to the inhibition effect of NO_2 formed in the reaction, the conversion data are treated according to previous procedure reported for NO oxidation on Pt-based catalysts to extract intrinsic activity data [12,41,42]. The previous studies show that the rate of NO oxidation is linearly proportional to the partial pressures of NO and O_2 and inversely proportional to that of NO_2 . When operating the reaction far below the thermodynamic equilibrium, the measured rate of NO conversion can be accurately described by Eq. (2). Based on the stoichiometry of NO oxidation, outlet partial pressures of NO, O_2 and NO_2 are quantitatively expressed by Eqs. (3–5).

$$r = k_1 \times \frac{p(\text{NO}) \times p(\text{O}_2)}{p(\text{NO}_2)} \quad (2)$$

$$p(\text{NO}) = (1 - X(\text{NO})) \times p(\text{NO})^0 \quad (3)$$

$$p(\text{O}_2) = \left(\frac{p(\text{O}_2)^0 - X(\text{NO}) \times p(\text{NO})^0}{2} \right) \quad (4)$$

$$p(\text{NO}_2) = X(\text{NO}) \times p(\text{NO})^0 \quad (5)$$

where k_1 , $X(\text{NO})$, $p(\text{NO})^0$ and $p(\text{O}_2)^0$ are the forward rate constant of NO oxidation, NO conversion, initial partial pressures of NO and O_2 , respectively.

For a plug flow reactor [43], Eq. (6) is valid.

$$\frac{m_{\text{cat}}}{\dot{n}} = \tau = \int_0^{X(\text{NO})} \frac{d(X(\text{NO}))}{r(X(\text{NO}))} \quad (6)$$

m_{cat} and \dot{n} are mass of the catalyst and molar flow rate of NO, respectively. By substituting $r(X(\text{NO}))$ in Eq. (6) by Eq. (2) and using Eqs. (2–5), we obtain Eq. (7). In order to derive the forward rate constant of NO oxidation at different temperatures, we have integrated the right hand side of this equation. To this end, the initial partial pressures of NO and O_2 of 4.10^{-4} and 1.10^{-1} bar, respectively, and the experimental NO conversion values determined at a modified contact time of $2.4 \cdot 10^5 \text{ g}_{\text{cat}} \text{ s mol}_{(\text{NO})}^{-1}$ are utilized.

$$\frac{m_{\text{cat}}}{\dot{n}} = \tau = \int_0^{X(\text{NO})} \frac{2 \times X(\text{NO}) \times d(X(\text{NO}))}{k_1 \times (1 - X(\text{NO})) \times (2 \times p(\text{O}_2)^0 - X(\text{NO}) \times p(\text{NO})^0)} \quad (7)$$

The obtained forward rate constant has a unit of $\text{mol}_{(\text{NO})} \text{ g}_{\text{cat}}^{-1} \text{ s}^{-1} \text{ bar}^{-1}$ and directly reflects the intrinsic NO oxidation activity of the catalysts. In contrast to the reaction rates, this constant allows us to correctly compare the activity of catalysts without requiring the partial pressure data of the reactants and reaction products. The Arrhenius dependence of the forward rate constant calculated for NO conversion not higher than 20% is plotted in Fig. 7(a). It is evident that the forward rate constant depends strongly on the catalysts. Astonishingly, Pt/Al/R catalyst aged under lean exhaust environment presents the highest constant followed by the fresh Pt/Al/F and thermally aged Pt/Al/O catalysts. It is worth noting that the forward rate constant of NO oxidation over P aged catalysts P/Pt/Al/R and P/Pt/Al/O is several orders of magnitude lower than over the P free counterparts, in particular below 150°C (Fig. 7). This is probably due to the fact that P clogs active surface Pt sites as evidenced by CO chemisorption, CO-DRIFTS and STEM-EDX (Fig. 6, Fig. S1 and Table 1). As a consequence, the number of surface Pt sites available for the reaction is decreased. This hypothesis is corroborated by the fact that the rate constant normalized by the total number of surface Pt atoms, estimated from the total amount of Pt and dispersion data (Table 1), narrows the activity differences between the catalysts P/Pt/Al/R, Pt/Al/R and Pt/Al/O (Fig. 7(b)). Despite this, the Pt/Al/R catalyst still shows the highest normalized rate constant as evident from Fig. 7(b).

In general, the observed differences in the activity of the catalysts can be attributed to the activation energies (E_a) for NO oxidation (Table 1). Pt/Al/R shows the lowest E_a of 95.6 kJ mol^{-1} followed by Pt/Al/F and Pt/Al/O with 112 and 115 kJ mol^{-1} , respectively. The lower E_a determined for Pt/Al/R may be related to the surface morphology of Pt nanoparticles evolved under simulated lean diesel operation conditions as evident from HR-TEM and CO-DRIFTS (Figs. 4 and 6). The presence of P increases the activation energy for NO oxidation from 95.6 to 127.7 and from 115 to $141.6 \text{ kJ mol}^{-1}$ for P/Pt/Al/R and P/Pt/Al/O, respectively. However in line with the corresponding P free catalysts, the E_a over the catalyst aged under lean exhaust environment (P/Pt/Al/R) is lower than that aged in air (P/Pt/Al/O). Based on the above discussion, one can suggest that lower the activation energy is, the higher the catalyst activity. However, this suggestion cannot be applied when a

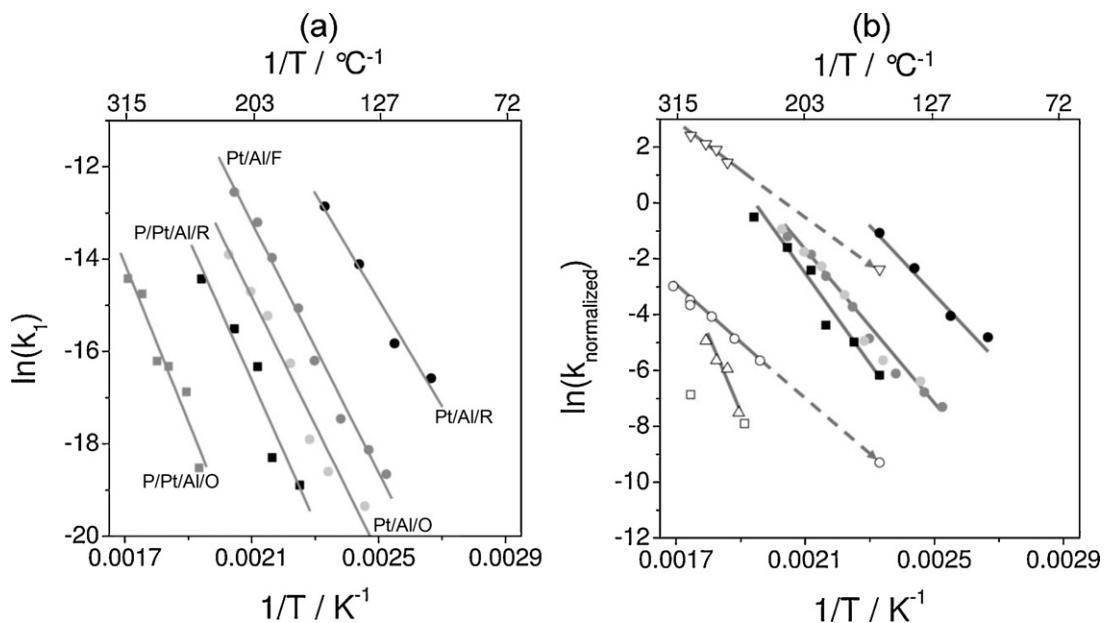


Fig. 7. Arrhenius plots of forward rate constant (k_1 in Eq. (2)) of NO oxidation (a) per catalyst amount and (b) per amount of surface Pt atoms over (●) Pt/Al/F, (●) Pt/Al/R, (●) Pt/Al/O, (●) P/Pt/Al/R, and (■) P/Pt/Al/O, (▽) Pt(0.3 wt%)/Al₂O₃ from [6], (△) Pt(0.27 wt%)/Al₂O₃ from [6], (□) Pt(0.1 wt%)/Al₂O₃ from [5], and (○) Pt(0.3 wt%)/Al₂O₃ [31]. Extrapolated data to 156 °C is shown with dash line in (b).

comparison is made between the present and previous studies as discussed below.

The activation energies determined in the present work for P free catalysts (Table 1) are higher than those reported (ca. 40 kJ mol⁻¹) in the literature for NO oxidation over Pt/Al₂O₃ without co-feeding of NO₂ [41,44]. Even after correcting their catalytic data with respect to the inhibiting effect of NO₂ on NO oxidation, the authors in reference [41] report activation energy of 82 kJ mol⁻¹, which is closer but still lower than that we report in this study (Table 1). The observed differences in the E_a may be due to the fact that previous studies were performed at higher temperatures (200–400 °C) as compared to that in the present study (see Fig. 7). In line with this, a decrease in the activation energy (of ca. 60 kJ mol⁻¹) is indeed observed above 160 and 200 °C for NO oxidation over Pt/Al/R and Pt/Al/F, respectively (see Fig. S2).

Another factor governing the activity is Pt dispersion and the particle size [5,6,8,45]. For example, it was reported that the NO oxidation activity (turnover rates) is increased by a factor of 100 upon decreasing the Pt dispersion from 82 to 4.4% on Al₂O₃ [6]. Similarly, activity increase by a factor of four was also observed by increasing the size of Pt particles (supported on Al₂O₃) from 2.4 to 7 nm [8]. We have verified if these structural characteristics of Pt are responsible for the observed high activity of Pt/Al/R (Fig. 7(a)). To this end, the activity data reported in the literature has been treated in the same way as in the present study as described above (Eqs. (2–7)) for deriving the forward rate constant of NO oxidation normalized by the total number of surface Pt atoms. In the present study the activity tests are performed at significantly lower temperatures than that reported, necessitating the extrapolation of the literature data to 156 °C (the highest temperature before the activation energy changes in our study, see Fig. S2) using the corresponding activation energy. The obtained normalized rate constant reflects the intrinsic activity of a single surface Pt atom and does not depend on the partial pressures of reactants and reaction products. Different catalysts can therefore be directly compared despite different reaction conditions such as varying NO, O₂ and NO₂ partial pressures. It can be clearly seen from Fig. 7(b) that the rate constant at 156 °C is ca. 3.2 times higher over Pt/Al/R than that on Pt(0.27 wt%)/Al₂O₃ with ca. 2 times lower Pt dispersion [6]. Furthermore, the constant

corresponding to Pt/Al/R is several orders of magnitude higher than that reported on other catalysts with significantly higher (>ca. factor of 4) Pt dispersion compared to that in Pt/Al/R (Table 1). Such a strong difference in the normalized rate constant (based on per available surface Pt atoms) cannot be simply attributed to the Pt loading that is ca. 10 times higher in Pt/Al/R than that in the previously reported Pt/Al₂O₃ catalysts (Table 1). The Pt/Al/F, Pt/Al/O and Pt/Al/R catalysts used in the present study contain identical Pt loading and similar sizes of Pt particles but significantly different surface Pt dispersion (Fig. 6 and Table 1). Based on the dispersion data, Pt/Al/O with lowest dispersion among the three catalysts would have shown the highest normalized rate constant of NO oxidation. However, it is evident from Fig. 7(b) that Pt/Al/O exhibits the normalized constant that is close to that of Pt/Al/F but is approximately 50 times lower than that of Pt/Al/R. From these observations it emerges that the Pt morphology plays an important role in NO oxidation. This is due to the fact that the exposed surface Pt particle facets and thus surface Pt sites are determined by particle morphology as evidenced by HR-TEM and CO-DRIFTS data of the catalysts. As a result of this, the intrinsic electronic and hence catalytic properties of surface Pt sites vary to different degrees on cuboctahedral (Pt (1 1 1) and (1 0 0) facets), truncated cube crystals (mainly (1 0 0) facets) and spherical (dominate with coordinatively unsaturated Pt sites) particles (inset of Fig. 4). Therefore, it can be suggested that the surface Pt sites of cuboctahedral particles are much more active for NO oxidation with O₂ than those on truncated cubes and spherical particles (Fig. 7 and Table 1). Additionally, the synergy between the (1 1 1) and (1 0 0) facets of cuboctahedral particles on the NO oxidation activity cannot be ruled out. This is in agreement with a recent theoretical study which concludes that the reaction predominantly occurs on the (1 1 1) planes without ruling out on the (1 0 0) terrace sites of Pt nanoparticles in the size range of 2.3 to 4.6 nm [3]. However, the authors also conclude that the reaction is Pt particle size dependent but irrespective of the Pt particle shape, which is different from our observations [3]. The size range of reported Pt nanoparticles is smaller than the average particle size determined in the present study by STEM (Table 1). Our results clearly demonstrate that the reaction is indeed sensitive to the morphology of Pt nanoparticles which evolve under these

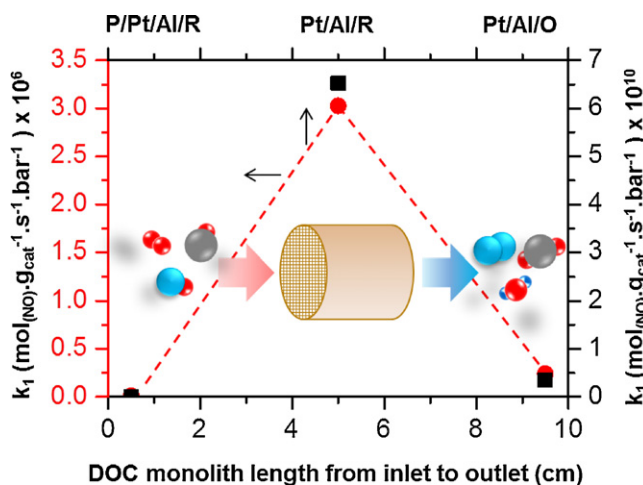


Fig. 8. NO conversion efficiency (in terms of forward rate constant (k_1)) at ca. 190 °C of the DOC monolith along the length (10 cm in length and 20 cm in diameter) is compared (black squares) with the corresponding model catalysts (red circles; data correspond to ca. 190 °C). DOC samples were taken at different length positions of the monolith. The DOC monolith was aged on a heavy duty small truck engine for 250 h under different driving profiles. Reaction conditions for the DOC samples are reported in [14]. (For interpretation of the references to color in this figure legend, the reader is referred to the web version of the article.)

experimental conditions. In contrast to the present study, the previously reported catalysts were treated under the same conditions (e.g., in air) [6,8]. This may have led to similar morphology of Pt nanoparticles in the catalysts and hence the observed differences in the activity.

Based on these results, the aging behavior and its influence on the NO conversion efficiency of a DOC monolith of a heavy duty small truck engine reported in [14] can be better understood (Fig. 8). The DOC_{in} , DOC_{mid} and DOC_{out} regions of the DOC monolith experience different aging environments (see cartoon in Fig. 8 and Section 1). The inlet and outlet regions experience chemical and thermal aging, respectively. Whereas, aging environment at the middle region can be unique as it comprises of both exhaust pollutants (propene, propane, CO, CO_2 , NO and O_2) and their products such as unburned hydrocarbons, CO_2 , H_2 and NO_2 . It almost excludes chemical contaminants (such as P, Zn). Therefore, the aging environment along the DOC monolith did influence the size, morphology and distribution of Pt particles [14]. This coincides well with that in the model catalysts $P/Pt/Al/R$, $Pt/Al/R$ and $Pt/Al/O$ which represent DOC_{in} , DOC_{mid} and DOC_{out} , respectively. The NO conversion efficiency (at ca. 190 °C under simulated diesel exhaust environment as reported in [14]) of these three regions of the DOC is compared with the corresponding NO oxidation activity (also at 190 °C) of model catalysts in terms of forward rate constants (units: $mol_{(NO)} g_{cat}^{-1} s^{-1} bar^{-1}$) derived from Eq. (2) in Fig. 8. Nonetheless, the comparison should be treated with caution and is only qualitative due to differences in the experimental conditions. It should be noted that the model catalysts exhibit several orders of magnitude higher k_1 values than that of DOC monolith samples. Significantly, DOC_{mid} exhibits the highest rate constant followed by the DOC_{out} and DOC_{in} . This activity trend matches very well with the model catalysts (as shown with red dash line in Fig. 8) indicating that the NO conversion efficiency of the DOC along the length can be attributed not only to the size but also to the morphology of Pt particles as discussed for model catalysts and also reported in [14] which is consistent with the literature [46,47]. For example, it is demonstrated that the NO conversion efficiency of $Pt(1\text{ wt\%})/Al_2O_3$ in the selective catalytic reduction (SCR) of NO with propene is a function of Pt dispersion [47]. The catalyst being pretreated

in SCR reaction mixture at 500 °C for 3 h presents the highest NO conversion with 35% Pt dispersion. This is followed by the catalyst pretreated in He at 200 °C for 3 h and heated to 400 °C in SCR mixture (10% Pt dispersion) and then the fresh catalyst calcined in air at 500 °C for 5 h (79% Pt dispersion). Interestingly, the activity trend is attributed to the proportion of redox active surface Pt sites which is higher for the catalyst with Pt dispersion of 35% followed by 10% and 79% as determined by Multitrack experiments [47]. This indicates that the chemical/catalytic properties of surface Pt sites are determined by the catalyst pretreatment conditions. These results corroborate our results very well and suggest that the reaction environment not only govern Pt dispersion but also particle morphology, which in turn determines the NO conversion efficiency of Pt nanoparticles. This study provides an unified concept on the aging behavior of a DOC and its influence on the NO conversion efficiency.

4. Conclusions

The influence of aging environment on the evolution (size, morphology and distribution) of Pt nanoparticles supported on alumina (model DOC) is studied to shed some light on the aging behavior of real DOC monoliths. Based on this study, the following main conclusions can be drawn:

- The evolution of Pt nanoparticles supported on alumina is indeed sensitive to the aging environment as evident from CO chemisorption, XRD, STEM, HR-TEM and CO-DRIFTS. Thermal aging in air at 800 °C resulted in the heterogeneous size, morphology and spatial distribution of Pt particles in $Pt/Al/O$. The morphology of Pt particles in the catalyst is mainly limited to truncated cubic and irregular shapes that exhibit predominantly (100) crystal planes as evident from CO-DRIFTS.
- Aging in lean diesel exhaust environment not only restricted the extensive growth of Pt particles (an average size of 5.5 nm) but also to a narrow size distribution and morphology predominantly to cubooctahedral in $Pt/Al/R$. The surface of these Pt nanoparticles tends to be dominated with (111) crystal planes as evidenced by HR-TEM and CO-DRIFTS.
- Phosphorus (a chemical contaminant) limited both the extensive growth of Pt particles and the morphology mainly to spherical shape irrespective of aging environment but this is more prominent under lean exhaust environment.
- NO oxidation activity in terms of the normalized forward rate constant (per surface Pt atoms) of the catalysts evidence that the reaction is indeed structure sensitive. $Pt/Al/R$ containing cubooctahedral Pt nanoparticles presents ca. 50 and 30 times higher constant value than that of $Pt/Al/F$ (spherical) and $Pt/Al/O$ (truncated cubic Pt particles), respectively.
- These results provide a basis for understanding the aging behavior and NO conversion efficiency along the length of a DOC monolith aged on a heavy duty small truck engine for 250 h.

Acknowledgments

The authors are thankful to Empa for financial support.

Appendix A. Supplementary data

Supplementary data associated with this article can be found, in the online version, at <http://dx.doi.org/10.1016/j.apcatb.2012.09.018>.

References

- [1] K. Hauff, U. Tuttles, G. Eigenberger, U. Nieken, Applied Catalysis B 100 (2010) 10.

[2] A.D. Smeltz, W.N. Delgass, F.H. Ribeiro, *Langmuir* 26 (2010) 16578.

[3] D. Mei, J. Du, M. Neurock, *Industrial and Engineering Chemistry Research* 49 (2010) 10364.

[4] R. Burch, P.J. Millington, *Catalysis Today* 26 (1995) 185.

[5] E. Xue, K. Seshan, J.R.H. Ross, *Applied Catalysis B* 11 (1996) 65.

[6] J.H. Lee, H.H. Kung, *Catalysis Letters* 51 (1998) 1.

[7] F.C. Galisteo, C. Larese, R. Mariscal, M. Lopez Granados, J.L.G. Fierro, R. Fernandez-Ruiz, M. Furio, *Topics in Catalysis* 30–31 (2004) 451.

[8] S.S. Mulla, N. Chen, L. Cumaranatunge, G.E. Balu, D.Y. Zemlyanov, W.N. Delgass, W.S. Epling, F.H. Ribeiro, *Journal of Catalysis* 241 (2006) 389.

[9] T. Kanerva, V. Kröger, K. Rahkamaa-Tolonen, M. Vippola, T. Lepistö, R.L. Keiski, *Topics in Catalysis* 45 (2007) 137.

[10] V. Kröger, T. Kanerva, U. Lassi, K. Rahkamaa-Tolonen, T. Lepistö, R.L. Keiski, *Topics in Catalysis* 42–43 (2007) 433.

[11] J. Andersson, M. Antonsson, L. Eurenus, E. Olsson, M. Skoglundh, *Applied Catalysis B* 72 (2007) 71.

[12] B.M. Weiss, E. Iglesia, *Journal of Physical Chemistry C* 113 (2009) 13331.

[13] D.D. Beck, C.J. Carr, *Journal of Catalysis* 110 (1988) 285.

[14] A. Winkler, D. Ferri, M. Aguirre, *Applied Catalysis B* 93 (2009) 177.

[15] W. Boll, S. Tischer, O. Deutschmann, *Industrial and Engineering Chemistry Research* 49 (2010) 10303.

[16] S. Benard, L. Retailleau, F. Gailleur, F. Gaillard, P. Vernoux, A.G. Fendler, *Applied Catalysis B* 55 (2005) 11.

[17] S. He, C. Sun, H. Du, X. Dai, B. Wang, *Chemical Engineering Journal* 141 (2008) 284.

[18] M. Santhosh Kumar, N. Hammer, M. Ronning, A. Holmen, D. Chen, J.C. Walmsley, G. Oye, *Journal of Catalysis* 261 (2009) 116.

[19] M.J. Rokosz, A.E. Chen, C.K. Lowe-Ma, A.V. Kucherov, D. Benson, M.C. Paputa Peck, R.W. McCabe, *Applied Catalysis B* 33 (2001) 205.

[20] M. Santhosh Kumar, E.H. Otal, M.H. Aguirre, A. Winkler, A. Ulrich, D. Rentsch, A. Weidenkaff, D. Ferri, *Catalysis Today* 184 (2012) 237.

[21] R.M. Rioux, H. Song, J.D. Hoefelmeyer, P. Yang, G.A. Somorjai, *Journal of Physical Chemistry B* 109 (2005) 2192.

[22] M. Santhosh Kumar, D. Chen, J.C. Walmsley, A. Holmen, *Catalysis Communications* 9 (2008) 747.

[23] S. Suhonen, M. Valden, M. Hietikko, R. Laitinen, A. Savimäki, M. Härkönen, *Applied Catalysis A* 218 (2001) 151.

[24] F.S. Shiau, T.T. Fang, *Materials Chemistry and Physics* 60 (1999) 91.

[25] A. Morlang, U. Neuhausen, K.V. Klementiev, F.H. Schütze, G. Miehe, H. Fuess, E.S. Lox, *Applied Catalysis B* 60 (2005) 191.

[26] L. Bendnarova, C.E. Lyma, E. Rytter, A. Holmen, *Journal of Catalysis* 211 (2002) 335.

[27] M.L. Toebe, Y. Zhang, J. Hajek, T.A. Nijhuis, J.H. Bitter, A.J. van Dillen, D.Y. Murzin, D.C. Koningsberger, K.P. de Jong, *Journal of Catalysis* 226 (2004) 215.

[28] A.K. Datye, *Journal of Catalysis* 216 (2003) 144.

[29] M. Cabie, S. Giorgio, C.R. Henry, M.R. Axet, K. Philippot, B. Chaudret, *Journal of Physical Chemistry C* 114 (2010) 2160.

[30] K.M. Bratlie, H. Lee, K. Komvopoulos, P. Yang, G.A. Somorjai, *Nano Letters* 7 (2007) 3097.

[31] C.Y. Chiu, Y. Li, L. Ruan, X. Ye, C.B. Murray, Y. Huang, *Nature Chemistry* 3 (2011) 393.

[32] S. Mostafa, F. Behafarid, J.R. Croy, L.K. Ono, L. Li, J.C. Yang, A.I. Frenkel, B.R. Cuenya, *Journal of the American Chemical Society* 132 (2010) 15714.

[33] K. McCrea, J.S. Parker, P. Chen, G. Somorjai, *Surface Science* 494 (2001) 238.

[34] R.M. Rioux, J.D. Hoefelmeyer, M. Grass, H. Song, K. Niesz, P. Yang, G.A. Somorjai, *Langmuir* 24 (2008) 198.

[35] J. Xu, J.T. Yates Jr., *Surface Science* 327 (1995) 193.

[36] C. Klunker, M. Balden, S. Lehwald, W. Daum, *Surface Science* 360 (1996) 104.

[37] J.A. Anderson, *Journal of the Chemical Society, Faraday Transactions* 88 (1992) 1197.

[38] M. Rivallan, E. Seguin, S. Thomas, M. Lepage, N. Takagi, H. Hirata, F. Thibault-Starzyk, *Angewandte Chemie-International Edition* 49 (2010) 785.

[39] M. Primet, J.M. Basset, M.V. Mathieu, M. Prettre, *Journal of Catalysis* 29 (1973) 213.

[40] R.G. Greenler, K.D. Burch, K. Kretzschmar, R. Klauser, A.M. Bradshaw, B.E. Hayden, *Surface Science* 152–153 (1985) 338.

[41] S.S. Mulla, N. Chen, W.N. Delgass, W.S. Epling, F.H. Ribeiro, *Catalysis Letters* 100 (2005) 267.

[42] N.A. Koryabkina, A.A. Phatak, W.F. Ruettinger, R.J. Farrauto, F.H. Ribeiro, *Journal of Catalysis* 217 (2003) 233.

[43] L.D. Schmidt, *The Engineering of Chemical Reactions*, Oxford University Press, New York, NY, USA, 2005, p. 618.

[44] L. Olsson, B. Westerberg, H. Persson, E. Fridell, M. Skoglundh, B. Andersson, *Journal of Physical Chemistry B* 103 (1999) 10433.

[45] L. Olsson, E. Fridell, *Journal of Catalysis* 210 (2002) 340.

[46] R.I. Masel, *Principles of Adsorption and Reaction on Solid Surfaces*, Wiley, New York, 1996.

[47] A.R. Vaccaro, G. Mul, J. Pérez-Ramírez, J.A. Moulijn, *Applied Catalysis B* 46 (2003) 687.